Evaluation of Aircraft Performance and Maneuverability by Computation of Attainable Equilibrium Sets

M. G. Goman,* A. V. Khramtsovsky,† and E. N. Kolesnikov‡
De Montfort University, Leicester, England LE1 9BH, United Kingdom

An aircraft's performance and maneuvering capabilities in steady flight conditions are usually analyzed considering the steady states of the rigid-body equations of motion. A systematic way of computation of the set of all attainable steady states for a general class of helical trajectories is presented. The proposed reconstruction of attainable equilibrium states and their local stability maps provides a comprehensive and consistent representation of the aircraft flight and maneuvering envelopes. The numerical procedure is outlined and computational examples of attainable equilibrium sets in the form of two-dimensional cross sections of steady-state maneuver parameters are presented for three different aircraft models.

Nomenclature

$\mathbf{A}, \mathbf{B}$	=	state and control matrices of the linearized system
$\mathbf{g}$	=	kinematical constraints vector function
$\mathbf{f}$	=	right-hand sides of aircraft rigid-body equations
$\mathbf{f_x}$	=	Jacobian matrix
H, M	=	altitude and Mach number
h_p	=	angular momentum of the engine rotors
p, q, r	=	body-axis angular rates
R	=	radius of helical trajectory
T	=	thrust force
V	=	flight velocity
$\mathbf{x}$	=	state vector
$\mathbf{y}_\mu$	=	maneuver parameter vector
α	=	angle of attack
β	=	angle of sideslip
γ	=	flight path angle
θ, ϕ	=	pitch and roll angles
$\delta_e, \delta_a, \delta_r$	=	elevator, aileron, and rudder deflections
δ_T	=	thrust throttle position
$\boldsymbol{\delta}$	=	control vector
$\boldsymbol{\Omega}$	=	total angular velocity
Ω_V	=	velocity-vector roll rate

Subscripts

ε	=	equilibrium
μ	=	maneuver

I. Introduction

THE evaluation of aircraft flight performance and maneuvering capabilities, from conceptual design to the final stage of flight clearance, is an important task of aircraft development. Flight performance reflects an aircraft's ability to perform steady coordinated maneuvers at different speeds and altitudes (e.g., its capability of maintaining a straight-and-level flight; a steady, level turn; climbing or gliding turns; etc.). The maneuverability characterizes an aircraft's ability to alter its steady flight trajectory via rotation with respect to the flight velocity vector. The level of maneuverability is directly linked with attainable values for the angle of attack or the normal load factor and the angular rate in the velocity-vector roll maneuver.

The steady performance and maneuvering capabilities are usually evaluated by solving the steady-state problem for the rigid-body equations of motion, which depend on the aircraft propulsion, aerodynamic, mass, and inertia characteristics [1–3]. The state and control parameters are interchangeable for the purpose of finding solutions to the steady-state problem. For example, the steady states can be determined for any particular combination of control inputs without setting any requirements for maneuver parameters. Alternatively, some steady-state and control variables can be chosen as independent, and the remaining variables can be determined according to the imposed kinematical constraints [2,4–6].

The continuation and bifurcation analysis methods first introduced in flight dynamics in the late seventies [7–10] have evolved into a powerful tool for aircraft trim and stability analysis [11]. Within this computational framework, the equilibrium states are computed in the extended space of state variables and one selected control parameter, whereas all other control effectors are kept constant. The steady states are represented as a one-parameter continuation diagram or as a two-dimensional equilibrium surface. At some ranges of control parameters, "folded" dependencies may appear in the steady-state diagrams and surfaces, which indicate potential nonlocal departures in motion variables at limit points of the folds. Other types of bifurcations or changes in steady-state local stability are also identified during the continuation procedure, thus allowing effective prediction of aircraft instability and loss of control. A number of important flight dynamics phenomena such as departures at high-incidence flight, onset of wing-rock motion, spin dynamics, and roll-coupled maneuvers have been successfully investigated using the continuation method [7–10,12–19].

Imposing additional maneuver-specific kinematical constraints, as was demonstrated in [4,5,20], allowed the continuation of steady states representing a specified maneuver. In this constrained problem, several control surfaces are deflected simultaneously so that this method can be used for designing aircraft steady-state maneuvers. The one-parameter continuation method, however, may be difficult and computationally intensive in reconstruction of all attainable steady states and the maneuver flight envelope, due to the nonuniqueness of solutions in the extended state and control parameter space.

The goal of this paper is to present a method for the reconstruction of an aircraft flight envelope considering a general class of steady

*Professor, Faculty of Engineering and Computing Sciences. Senior Member AIAA.
†Visiting Research Fellow, Faculty of Engineering and Computing Sciences.
‡Currently Engineer, Flight Sciences, Bombardier Aéronautique, 400 Côte-Vertu, Montréal, H4S 1Y9, Canada.

maneuvers via computation of the set of all attainable steady states. The results are represented in the state and maneuver parameters space, whereas the associated control parameters are stored in a special data structure for processing and analysis at a later stage. Steady states are computed for the equations of motion augmented by a number of auxiliary equations specifying maneuver kinematics. The set of all attainable equilibrium states is computed on a grid of state and maneuver parameter points and visualized in the form of two-dimensional cross sections. The local stability maps, reflecting the structure of the eigenvalues of the linearized equations of motion, complement this representation.

The next section of this paper discusses equations of spatial motion and kinematics of steady-state solutions. The proposed computational method is presented in Sec. III. Section IV contains a number of examples of two-dimensional attainable equilibrium sets and local stability maps for the open-loop mathematical models for the F-18 HARV, F-16, and F-14 aircraft, based on data from [21–24].§ Section V summarizes the main results and presents our conclusions.

II. Equations of Motion

The rigid aircraft equations of motion can be presented in the form of a set of nonlinear, autonomous, ordinary differential equations describing rotational/translational accelerations and rotational kinematics using Euler angles. These equations have the following form [10]:

$$\begin{bmatrix} \dot{p} \\ \dot{q} \\ \dot{r} \end{bmatrix} = \begin{bmatrix} I_x & 0 & -I_{xz} \\ 0 & I_y & 0 \\ -I_{xz} & 0 & I_z \end{bmatrix}^{-1} \begin{bmatrix} (I_y - I_z)qr + \bar{q}SbC_l \\ (I_z - I_x)pr + \bar{q}S\bar{c}C_m + h_p r \\ (I_x - I_y)pq + \bar{q}SbC_n - h_p q \end{bmatrix}$$

$$(1)$$

$$\dot{\alpha} = q - (p\cos\alpha + r\sin\alpha)\tan\beta$$
$$- \frac{\bar{q}S}{mV}(C_x\sin\alpha - C_z\cos\alpha)\sec\beta - \frac{T\sin\alpha\sec\beta}{mV}$$
$$+ \frac{g}{V}(\cos\theta\cos\phi\cos\alpha + \sin\theta\sin\alpha)\sec\beta \qquad (2)$$

$$\dot{\beta} = p\sin\alpha - r\cos\alpha$$
$$- \frac{\bar{q}S}{mV}(C_x\cos\alpha\sin\beta - C_y\cos\beta + C_z\sin\alpha\sin\beta)$$
$$- \frac{T\cos\alpha\sin\beta}{mV} + \frac{g}{V}(\cos\theta\sin\phi\cos\beta$$
$$+ \sin\theta\sin\beta\cos\alpha - \cos\theta\cos\phi\sin\beta\sin\alpha) \qquad (3)$$

$$\frac{\dot{V}}{V} = \frac{\bar{q}S}{mV}(C_x\cos\alpha\cos\beta + C_y\sin\beta + C_z\sin\alpha\cos\beta)$$
$$+ \frac{T}{mV}\cos\alpha\cos\beta + \frac{g}{V}(\sin\theta\cos\alpha\cos\beta + \cos\theta\sin\phi\sin\beta$$
$$+ \cos\theta\cos\phi\sin\alpha\cos\beta) \qquad (4)$$

$$\dot{\theta} = q\cos\phi - r\sin\phi \qquad (5)$$

$$\dot{\phi} = p + (q\sin\phi + r\cos\phi)\tan\theta \qquad (6)$$

$$\dot{\psi} = (q\sin\phi + r\cos\phi)\sec\theta \qquad (7)$$

where I_x, I_y, I_z, and I_{xz} are the moments of inertia; $\bar{q} = \rho V^2/2$ is the dynamic pressure; V is the airspeed; ρ is the air density; S is the wing

§Data available online at http://www.nasa.gov/centers/dryden/history/pastprojects/HARV/Work/NASA2/nasa2.html [retrieved 9 Dec. 2007].

reference area; b is the wing span; $\bar{c}$ is the mean aerodynamic chord of the wing; g is the gravitational acceleration; and m is the aircraft mass.

In general, the nondimensional aerodynamic force $C_{x,y,z}$ and moment $C_{l,m,n}$ coefficients depend nonlinearly on angle of attack α and sideslip angle β; angular velocity-vector components p, q, and r; elevator, aileron, and rudder deflections δ_e, δ_a, and δ_r; and Mach number M. The static thrust T depends nonlinearly on altitude H, Mach number M, and throttle position δ_T.

The aerodynamic coefficients and the thrust force are usually defined as tabular functions of the motion parameters and control inputs. The lookup data tables used for interpolating the aerodynamic coefficients are obtained from static, forced oscillations and rotary-balance wind-tunnel tests. The tabulated data are interpolated using linear or cubic spline function approximations, depending on requirements for smoothness of the aerodynamic coefficient functions.

The first six equations (1–6) can be expressed in the general class of helical trajectories with rotation around a vertical axis [1]. In this motion, the aerodynamic pressure distribution, the integrated forces and moments, and the gravity projections are all constant with time in the rigid-body frame of reference. The steady-state conditions are characterized by the state vector, composed of motion variables in the selected reference frames, and the control vector, composed of aerodynamic surface deflections and throttle position. This description of a steady-state motion may be expanded by a number of parameters, characterizing maneuver kinematics. These parameters include the flight path angle

$$\sin\gamma = \cos\alpha\cos\beta\sin\theta - \sin\beta\sin\phi\cos\theta - \sin\alpha\cos\beta\cos\phi\cos\theta$$
$$(8)$$

the steady turning rate Ω, or the radius R of the helical trajectory, which are related as $\Omega = (V\cos\gamma)/R$ (see Fig. 1a). The kinematical triad V, γ, and Ω (or V, γ, and R) completely specifies the helical
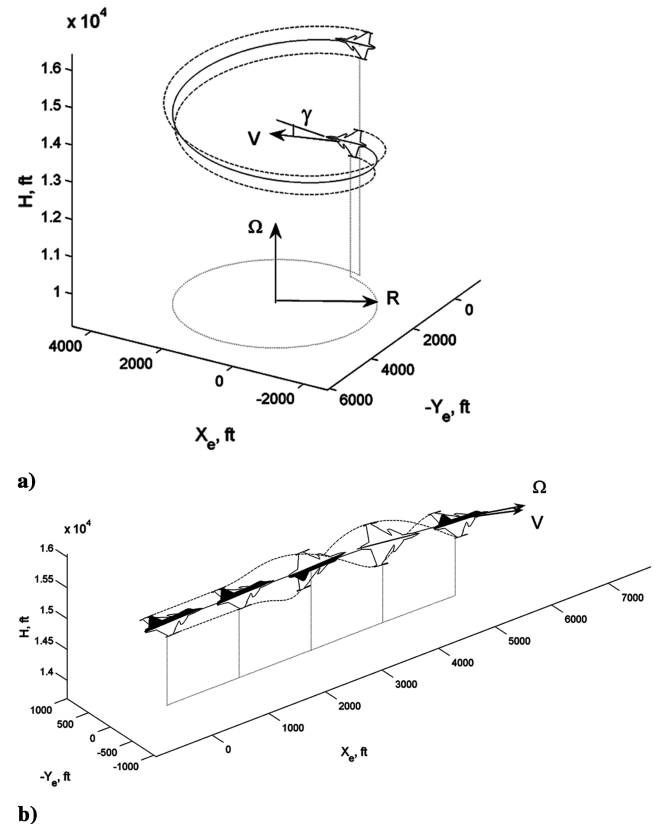

Fig. 1 Steady-state maneuvers used for aircraft performance and maneuverability evaluation: a) kinematics of steady-state helical motion and b) velocity-vector roll maneuver.

trajectory [16]. The yaw angle in steady helical motion varies with time and its time derivative defines the steady turning rate $\dot{\psi} = \Omega$, which can be expressed [Eq. (7)] along with the radius of steady helical trajectory R through the state variables as follows:

$$\Omega = (q \sin\phi + r \cos\phi) \sec\theta \qquad (9)$$

$$R = \frac{V \cos\gamma \cos\theta}{q \sin\phi + r \cos\phi} \qquad (10)$$

The steady helical motion may be a straight-and-level flight with $\Omega = 0$ and $\gamma = 0$ or a level turn with $\gamma = 0$ and $\Omega \neq 0$. Note that aircraft steady-spin motion is also a helical solution of systems (1–6). It is characterized by a high angle of attack, very small trajectory radius comparable with the wing span ($R/b \approx 1$), and near-vertical flight path angle $\gamma \approx -\pi/2$.

The first eight equations (1–6) can be expressed in the general form of a nonlinear first-order vector differential equation:

$$\dot{\mathbf{x}} = \mathbf{f}(\mathbf{x}, \boldsymbol{\delta}), \qquad \mathbf{x} \in X \subset \Re^8, \qquad \boldsymbol{\delta} \in U \subset \Re^4 \qquad (11)$$

where the aircraft state vector $\mathbf{x} = (p, q, r, \alpha, \beta, V, \theta, \phi)^T$ is composed of the angular velocity components in the body-fixed reference frame (p, q, r), the linear velocity components in the wind-body reference frame (α, β, V), and the two Euler angles (θ, ϕ). The aircraft state vector $\mathbf{x}$ belongs to the bounded region X, specified by the validity of the aerodynamic model and the imposed constraints on the aerodynamic loads. The control vector $\boldsymbol{\delta} = (\delta_e, \delta_a, \delta_r, \delta_T)^T$ is composed of control surface deflections $(\delta_e, \delta_a, \delta_r)$ and throttle position δ_T. It belongs to the bounded region U, which is specified by control deflection limits $\delta_{i\min} \leq \delta_i \leq \delta_{i\max}$, where $i = e, a, r, T$.

The attainable turning rate in steady helical motion is normally much lower than the maximum roll rate attainable in intensive maneuvering [25]. For example, during intensive rotation in roll, shown in Fig. 1b, the state variables of Eq. (11) can be approximated by a sum of pseudosteady mean values and superimposed small-amplitude oscillations produced by harmonic gravity projections in the body-fixed axes. The pseudosteady components can be analyzed as steady states of the reduced fifth-order system for the first five state variables $\mathbf{x} = (p, q, r, \alpha, \beta)^T$ and the reduced control vector $\boldsymbol{\delta} = (\delta_e, \delta_a, \delta_r)^T$ [26]. The flight velocity is assumed constant and the gravitational force is neglected. The steady states of this fifth-order dynamic system are analyzed in Sec. IV for evaluation of attainable values for the angle of attack, sideslip, and velocity-vector roll rate $\Omega_V = p \cos\alpha \cos\beta + q \cos\alpha \sin\beta + r \sin\alpha \cos\beta$ (the projection of the total angular velocity vector $\boldsymbol{\Omega}$ on the velocity vector V). Note that the steady-state solution of the reduced fifth-order system also corresponds to a helical trajectory, but with an axis arbitrarily oriented in space.

The investigation of the steady states of system (11) and the reduced fifth-order subsystem constitutes a fundamental problem in flight dynamics. The steady states are important for determining sustainable performance and maneuvering capabilities: they can be used as initial conditions for flight simulation and for linearization of the aircraft nonlinear dynamics. Because the steady states are characterized by zero rate of change of the linear and angular velocity components in the selected reference frames, the steady-state problem is formulated by setting all time derivatives in the equations of motion equal to zero and solving the resulting set of nonlinear algebraic equations:

$$\mathbf{f}(\mathbf{x}_\varepsilon, \boldsymbol{\delta}_\varepsilon) = 0, \qquad \mathbf{x}_\varepsilon \in X \subset \Re^n, \qquad \boldsymbol{\delta}_\varepsilon \in U \subset \Re^m \qquad (12)$$

where $\mathbf{x}_\varepsilon$ and $\boldsymbol{\delta}_\varepsilon$ are the steady-state vector and trim control vector, respectively.

For small state and control vector perturbations, $\Delta\mathbf{x} = \mathbf{x} - \mathbf{x}_\varepsilon$ and $\Delta\boldsymbol{\delta} = \boldsymbol{\delta} - \boldsymbol{\delta}_\varepsilon$, the equations of motion (11) can be approximated by the linear time-invariant system

$$\Delta\dot{\mathbf{x}} = \mathbf{A}\Delta\mathbf{x} + \mathbf{B}\Delta\boldsymbol{\delta} \qquad (13)$$

where

$$\mathbf{A} = \mathbf{f}_\mathbf{x}(\mathbf{x}_\varepsilon, \boldsymbol{\delta}_\varepsilon), \qquad \mathbf{B} = \mathbf{f}_\delta(\mathbf{x}_\varepsilon, \boldsymbol{\delta}_\varepsilon)$$

are the state and control matrices, respectively. A steady state $\mathbf{x}_\varepsilon$ is locally stable if the real parts of all the eigenvalues of the $\mathbf{A}$ matrix are negative. If the real part of any eigenvalue of the $\mathbf{A}$ matrix is positive, the steady state is locally unstable. The system is attracted to a stable steady state in its neighborhood and repelled if the steady state is unstable. The eigenvectors of the $\mathbf{A}$ matrix characterize subspaces for different modes of disturbed motion. The linearized response to control input $\Delta\boldsymbol{\delta}$ is characterized by the control $\mathbf{B}$ matrix. The $\mathbf{A}$ and $\mathbf{B}$ matrices calculated on a grid of points for different flight regimes and steady maneuvers provide a linear parameter-varying approximation for the original nonlinear system (11), which is equally important for the open-loop dynamics analysis and for control law design.

Variation of flight regime and/or maneuver parameters can lead to various bifurcational changes in the dynamics of system (11). Local bifurcations can be identified via changes in the eigenvalues of the linearized system (13). More information on dynamic systems theory and qualitative and bifurcation analyses can be found in [27].

III.   Computation of Attainable Equilibrium Sets

A systematic reconstruction of all the attainable equilibrium states is described in this section as a method for evaluation of aircraft performance and maneuvering flight envelopes. The computational problem for steady states is formulated for equations of motions, augmented by auxiliary equations specifying maneuver kinematics and maneuver parameters. The solutions of this constrained trim problem are presented in the form of attainable equilibrium sets computed on a grid of points in the plane of two selected parameters characterizing the flight regime and steady maneuver. All steady states are classified according to the eigenvalue spectrum of the linearized system (13). This classification generates local stability maps, giving a qualitative insight into the aircraft nonlinear dynamics. For every steady state in the $\mathbf{A}$ and $\mathbf{B}$ matrices of the linearized system (13), the eigenvalues and eigenvectors of the Jacobian matrix $\mathbf{A}$ are stored in a special data structure, along with the trim control parameters, so that they can be easily retrieved for later detailed analysis.

Deflection constraints on aircraft control inputs limit the available control power so that the set of equilibrium states for the system described by Eq. (11) is bounded. The set of attainable equilibrium states S_ε incorporates all possible trim states generated by the available bounded control $\boldsymbol{\delta} \in U$ in the allowable region of state variables $\mathbf{x} \in X$ and is defined as

$$S_\varepsilon = \{\mathbf{x}_\varepsilon : \mathbf{f}(\mathbf{x}_\varepsilon, \boldsymbol{\delta}_\varepsilon) = 0, \ \mathbf{x}_\varepsilon \in X \subset \Re^n, \ \boldsymbol{\delta}_\varepsilon \in U \subset \Re^m\} \qquad (14)$$

The attainable equilibrium states in Eq. (14) belong to a wide class of aircraft steady helical trajectories with a vertical axis of rotation when $n = 8$ and with an arbitrary oriented axis when $n = 5$. Some additional kinematical constraints are required to specify a particular steady maneuver for performance or maneuverability evaluation.

A.   Constrained Trim Formulation

Every steady maneuver from the complete set of equilibrium solutions (14) may be additionally characterized by a vector of kinematical parameters, $\mathbf{y}_\mu \in \Re^k$ [see Eqs. (8–10)], which is functionally linked with the state vector $\mathbf{y}_\mu = \mathbf{g}(\mathbf{x})$. To determine the required trim control vector $\boldsymbol{\delta}_\varepsilon$ and the equilibrium state vector $\mathbf{x}_\varepsilon$ for a particular maneuver, specified by parameter vector $\mathbf{y}_\mu$, the following augmented system of trim equations should be solved:

$$\begin{aligned} \mathbf{f}(\mathbf{x}_\varepsilon, \boldsymbol{\delta}_\varepsilon) = 0, \qquad \mathbf{f} \in \Re^n, \qquad \mathbf{x}_\varepsilon \in X \subset \Re^n \\ \mathbf{y}_\mu = \mathbf{g}(\mathbf{x}_\varepsilon), \qquad \boldsymbol{\delta}_\varepsilon \in U \subset \Re^m, \qquad \mathbf{g} \in \Re^k \end{aligned} \qquad (15)$$

where k-dimensional ($k \leq m$) vector function $\mathbf{g}$ defines the required maneuver. When the number of constraints in Eq. (15) equals the number of control parameters (i.e., $k = m$), system (15) represents a set of ($n + m$) equations with ($n + m$) unknowns. This means that

for every particular maneuver specified by vector $\mathbf{y}_\mu$, there exists an isolated solution of system (15) consisting of steady-state vector $\mathbf{x}_\varepsilon$ and control vector $\boldsymbol{\delta}_\varepsilon$. When $k < m$, the solution of augmented trim system (15) will not be unique and isolated, and the $m - k$ free control parameters can be used for continuation along the $(m - k)$-dimensional manifold of equilibrium solutions.

In the trimming procedure for system (12), the control input $\boldsymbol{\delta}_\varepsilon$ is known a priori, whereas in system (15), the trim control vector $\boldsymbol{\delta}_\varepsilon$ is defined implicitly by the augmented system of $n + k$ equations. In Eq. (12), $\boldsymbol{\delta}_\varepsilon$ is the input vector and $\mathbf{x}_\varepsilon$ is to be determined. In Eqs. (15), maneuver specification $\mathbf{y}_\mu$ is the input vector, whereas steady state $\mathbf{x}_\varepsilon$ and trim control $\boldsymbol{\delta}_\varepsilon$ are to be determined. The equilibrium state vector $\mathbf{x}_\varepsilon$ and corresponding trim control vector $\boldsymbol{\delta}_\varepsilon$ can be determined on a grid of points in the maneuver parameter space $\mathbf{y}_\mu$, allowing the reconstruction of the steady flight envelopes, in which boundaries are specified by bounded regions X and U.

The vector function $\mathbf{g}$ and the parameter vector $\mathbf{y}_\mu$ in Eq. (15) specify the maneuver type and the maneuver kinematical parameters, respectively. To have a unique isolated solution in Eq. (15), when $n = 8$ and $m = 4$, requires four different constraints. A helical trajectory with a vertical axis can be described by three kinematical parameters such as flight velocity V, flight path angle γ, and either the turn radius R or the angular rate Ω [see Eqs. (8–10)]. One additional constraint can be imposed on aircraft attitude to complete the trim problem, such as a prescribed value for the sideslip angle β or for the roll angle ϕ. So the full vector of constraint functions can be selected as one of the following combinations: 1) $\mathbf{g} = (V, R, \gamma, \beta)^T$, 2) $\mathbf{g} = (V, \Omega, \gamma, \beta)^T$, 3) $\mathbf{g} = (V, R, \gamma, \phi)^T$, or 4) $\mathbf{g} = (V, \Omega, \gamma, \phi)^T$. The steady straight-and-level flight, for example, can be defined by vector $\mathbf{y}_\mu = (V_\mu, \Omega_\mu = 0, \gamma_\mu = 0, \beta_\mu)^T$ and the steady, level turn can be defined by vector $\mathbf{y}_\mu = (V_\mu, R_\mu, \gamma_\mu = 0, \beta_\mu)^T$. The functional representations for γ, R, and Ω are given in Eqs. (8–10). The velocity, sideslip, and roll angle (V, β, and ϕ) are the components of the state vector $\mathbf{x}$; hence, the kinematical constraints can be expressed in a straightforward form: $V = V_\mu$, $\beta = \beta_\mu$, and $\phi = \phi_\mu$.

For analyzing steady states in the velocity-vector roll maneuver, system (11) is considered for $\mathbf{x} = (\alpha, \beta, p, q, r)^T$ and $\boldsymbol{\delta} = (\delta_e, \delta_a, \delta_r)^T$, the reduced state and control vectors, respectively. To have a unique isolated solution, the constrained trim formulation (15) should include three kinematical constraints: for example, $\mathbf{g} = (\alpha, \beta, \Omega_V)^T$ or, alternatively, $\mathbf{g} = (n_z, n_y, \Omega_V)^T$, where n_z and n_y are the normal and side load factors, respectively. In the latter case, the constraint vector function will also depend on control input $\mathbf{g}(\mathbf{x}, \boldsymbol{\delta})$. The constraint equations for the investigation of the velocity-vector roll maneuver will have the following form: $\alpha = \alpha_\mu$, $\beta = \beta_\mu$, and $p \cos \alpha \cos \beta + q \cos \alpha \sin \beta + r \sin \alpha \cos \beta = \Omega_{V\mu}$. The two other projections of angular velocity vector in the wind-body axes are defined as function of α, β, and Ω_V. Solution of system (15) in this case will again be unique and isolated, because the dimension of control vector $\boldsymbol{\delta} = (\delta_e, \delta_a, \delta_r)^T$ is equal to the number of constraint equations.

B. Computational Procedure

The constrained trim problem (15) is solved numerically using the Newton–Raphson method:

$$\begin{vmatrix} \mathbf{x}_\varepsilon^{k+1} \\ \boldsymbol{\delta}_\varepsilon^{k+1} \end{vmatrix} = \begin{vmatrix} \mathbf{x}_\varepsilon^k \\ \boldsymbol{\delta}_\varepsilon^k \end{vmatrix} - \begin{bmatrix} \mathbf{f_x} & \mathbf{f_\delta} \\ \mathbf{g_x} & \mathbf{g_\delta} \end{bmatrix}^{-1} \begin{vmatrix} \mathbf{f}(\mathbf{x}_\varepsilon^k, \boldsymbol{\delta}_\varepsilon^k) \\ \mathbf{g}(\mathbf{x}_\varepsilon^k, \boldsymbol{\delta}_\varepsilon^k) - \mathbf{y}_\mu \end{vmatrix} \qquad (16)$$

where matrices $\mathbf{f_x}$, $\mathbf{f_\delta}$, $\mathbf{g_x}$, and $\mathbf{g_\delta}$ are evaluated numerically. The convergence process is terminated when all components of the increment vectors $\Delta \mathbf{x}_\varepsilon^k = \mathbf{x}_\varepsilon^{k+1} - \mathbf{x}_\varepsilon^k$ and $\Delta \boldsymbol{\delta}_\varepsilon^k = \boldsymbol{\delta}_\varepsilon^{k+1} - \boldsymbol{\delta}_\varepsilon^k$ become less than some prescribed accuracy levels $\Delta x_i^k / (x_{i\,\max} - x_{i\,\min}) \ll \varepsilon_i$ and $\Delta \delta_j^k / (\delta_{j\,\max} - \delta_{j\,\min}) \ll \varepsilon_j$, respectively. The convergence process is also terminated if the accuracy criteria have not been met after a preset maximum number of iterations. Note that an alternative way of solving this problem is described in [2] using a scalar cost function and a function-minimization algorithm.

For every new maneuver parameter vector $\mathbf{y}_\mu$, the initial guess for solution $\mathbf{x}_\varepsilon^0$, $\boldsymbol{\delta}_\varepsilon^0$ is taken equal to a successful solution obtained for the previous value of parameter vector $\mathbf{y}_\mu$. In computation of the starting solution of system (15), the modules for increments of the state and control vectors during the iterative process are confined by some preset values, but the maximum number of iterations is increased.

Maneuver parameter vector $\mathbf{y}_\mu$ is classified as attainable if the steady-state vector $\mathbf{x}_\varepsilon$ and trim control vector $\boldsymbol{\delta}_\varepsilon$ have successfully converged to the internal points of the bounded regions X and U, respectively. If during the Newton–Raphson iterations the state vector $\mathbf{x}_\varepsilon$ is pushed out of the region X or the control vector $\boldsymbol{\delta}_\varepsilon$ is saturated on the boundary of the region U, further reduction of the error norms becomes impossible. In this case, the selected maneuver parameter $\mathbf{y}_\mu$ is classified as unattainable. Note that after successful convergence, the iterative algorithm (16) automatically provides the state and control matrices for the linearized system (13).

To represent multidimensional set of all equilibrium states S_ε [Eq. (14)], two-dimensional cross sections are computed for different fixed values of the other flight regime and maneuver parameters. These cross sections, or attainable equilibrium sets, are computed on a square grid of points with spacing to allow accurate representation of external boundaries and boundaries for internal regions of steady states with different local dynamics. The grid points with attainable steady-state parameters are displayed using different markers reflecting their local stability properties, and the remaining grid points are left unmarked. The marked area on a selected grid approximates the two-dimensional cross section of the attainable equilibrium set and provides a local stability map for attainable equilibria [28]. The steady-state local stability properties are defined by the eigenvalues of the system $\mathbf{A}$ matrix in Eq. (13).

A set of markers, shown in Fig. 2, was selected to visualize the local stability of steady-state solutions. Stable steady states are marked by solid circles, whereas for unstable steady states, several different markers are used to reflect topology of the local dynamics:

1) Saddle points, or aperiodically unstable equilibria with one positive real eigenvalue, are marked by ×.

2) Unstable focuses, or oscillatory unstable equilibria with unstable complex conjugate pair of eigenvalues, are marked by ○.

3) Unstable nodes, or equilibria with two positive real eigenvalues, are marked by *.

4) Saddle-focus points, or equilibria with three unstable eigenvalues (one real and one complex conjugate pair), are marked by ◇.

5) Saddle-node points, or equilibria with three unstable real eigenvalues, are marked by ☆.

For each marked grid point, all computed data for a given steady state are stored in a special data structure for later use and visualization. The stored data include the state vector $\mathbf{x}_\varepsilon$ and associated trim control vector $\boldsymbol{\delta}_\varepsilon$, the state and control matrices of the linearized system (13), and the eigenvalues and the eigenvectors of the $\mathbf{A}$ matrix.

IV. Computational Results

The mathematical models for the F-18 HARV, F-16, and F-14 aircraft (corresponding geometric, mass, inertia, and aerodynamic data can be found in [21–24]¶) are used here as the case studies for testing the proposed computational method. The presented analysis is limited by consideration of the bare-airframe models without inclusion of the stability and control augmentation system. The computation of attainable equilibrium sets of the closed-loop system may be a useful method for postdesign validation of control laws, but this is beyond the scope of this paper. The example of such closed-loop system analysis is presented in [29] for the ADMIRE model of a rigid small fighter aircraft with a delta–canard configuration with the nonlinear dynamic inversion control law.

The computation of attainable regions for a class of steady helical trajectories using the eighth-order system (11) was performed only for the first aircraft model, whereas the investigation of attainable

---

¶Data available online at http://www.nasa.gov/centers/dryden/history/pastprojects/HARV/Work/NASA2/nasa2.html [retrieved 9 Dec. 2007].
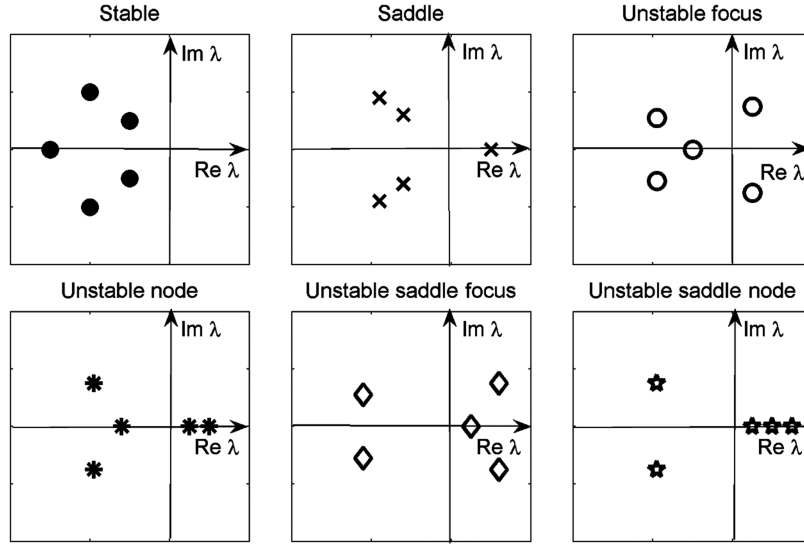
Fig. 2 Qualitative classification of the eigenvalues spectrum.

equilibrium sets using the reduced fifth-order system (11) was performed for all three aircraft models.

A. Aircraft A

The source of aerodynamic data, mass, and inertia parameters for the F-18 HARV aircraft is a simplified model** that is nonlinear with respect to angle of attack and is linear with respect to all other state variables and control surface deflections. The model is valid for small velocities ($M \leq 0.6$) and covers a wide range of angles of attack (-14 to 90 deg). The reference center-of-gravity position is $x_{cg} = 0.25\bar{c}$.

Figures 3a and 3b show the altitude–Mach-number flight envelope for a steady, level turn ($\gamma = 0$) with $R = 800$ m and $\beta = 0$. The boundary of this flight envelope at high Mach numbers is specified by maximum throttle position ($\delta_T = \delta_{T\,\text{max}}$); the angle of attack at this boundary is small ($\alpha \approx 10$ deg), and the roll angle is very high ($\phi \approx 80$ deg).

The low-Mach-number boundary corresponds to saturated deflection of the elevator ($\delta_e = \delta_{e\,\text{min}}$); the angle of attack at this boundary is very high ($\alpha \approx 50$ deg) and the roll angle is moderate ($\phi \approx 30$ deg). The regions for attainable steady maneuvers with right rotation (Fig. 3a) and with left rotation (Fig. 3b) are practically identical, but the local stability maps are different. The left level turns (Fig. 3b) are more stable than the right level turns (Fig. 3a), due to the effect of the engine rotors. The angular momentum of the engine rotors ($h_p = 15,000$ kg $\cdot$ m^2/s) destabilizes the slow phugoid and spiral motion modes in maneuvers with right rotation.

The eigenvalues of steady, level turns with left rotation are shown in Fig. 3c for two different flight regime points. At $M = 0.6$ and $H = 1.5$ km, the eigenvalues (solid circles) are all stable, including the spiral and phugoid modes. At the left boundary of flight envelope ($M = 0.15$ and $H = 1.5$ km), the eigenvalues (open circles) indicate slower dynamics in all modes and oscillatory instability of the phugoid mode.

The attainable set of all steady turns is presented in Fig. 3d for flight-envelope point $H = 5$ km and $M = 0.4$. The attainable maneuvers are reconstructed in the plane of flight path angle γ and turning angular rate Ω. The attainable set includes ascending and descending straight trajectories on a segment $\Omega = 0$ and -8 deg $< \gamma < 30$ deg, level turns on a segment $\gamma = 0$ and $|\Omega| \leq 9$ deg/s, and climbing ($\Omega \neq 0$ and $\gamma > 0$) and gliding ($\Omega \neq 0$ and $\gamma < 0$) helical trajectories. Helical trajectories with negative rotation are relatively more stable than helical trajectories with opposite rotation, due to the effect of the engine rotors. The right

and left boundaries of the attainable region correspond to the maximum ($\delta_T = \delta_{T\,\text{max}}$) and zero throttle ($\delta_T = 0$) positions, respectively. Two "sleeves" of the attainable region at negative path angles indicate attainable "steep-dive" maneuvers, which can be stable or unstable, depending on the path angle and turning angular rate.

Four different cross sections of the attainable equilibrium states of the reduced fifth-order system (11) are presented in Figs. 4a–4d for flight regime $H = 5$ km and $M = 0.4$. The first cross section (Fig. 4a) shows the attainable region for steady states in the plane of angle of attack α and sideslip angle β when the velocity-vector roll rate is kept at a zero value ($\Omega_V = 0$). The rotation vector in this case is normal to the linear velocity vector and the aircraft follows a complete loop, with the radius $R = mV^2/L$ and angular rate $\Omega = L/mV$, where L is the lift force (the side force D is assumed equal to zero). At nonzero value $\Omega_V \neq 0$, the loop is transformed into a helical trajectory. The radius of this helical trajectory will decrease with increase of Ω_V (see Fig. 1b).

The second cross section (Fig. 4b) shows the attainable region for angle of attack α and the velocity-vector roll rate Ω_V at zero value of sideslip angle ($\beta = 0$). The last two cross sections (Figs. 4c and 4d) show the attainable regions for the velocity-vector roll rate Ω_V and sideslip angle β at two values of angle of attack: $\alpha = 10$ and 20 deg, respectively.

Each boundary of attainable steady-state region, presented in Figs. 4a–4d, is associated with saturation of one of the control surfaces (i.e., rudder, aileron, or elevator). The trim control inputs at the boundary clearly indicate the control surface that limits the expansion of the attainable region. Characterization of local stability of steady states using different markers (see Fig. 2) provides a basis for prediction of aircraft dynamics at different combinations of control inputs. For example, aircraft A is stable at low angles of attack ($\alpha < 27^0$) and moderate values of rotation rate ($|\Omega_V| \leq 60$ deg/s and 8 deg $< \alpha < 20$ deg) (Figs. 4a and 4b). Maneuvers with an intensive rate of rotation ($|\Omega_V| > 60$ deg/s and 8 deg $< \alpha < 20$ deg) become oscillatory unstable, due to the destabilizing effect of nonlinear inertia coupling terms in Eq. (1).

Note that the accumulated data for trim control values and eigenvalues of the steady states can be used for dynamics analysis in a way similar to the continuation and bifurcation analysis methods. Figures 5a and 5b present trim deflections of the control surfaces and the locus of eigenvalues stored in a special data structure for the maneuver specified in Figs. 4b and 4c by the horizontal and vertical arrows, respectively. The maneuver holds the angle of attack and sideslip constant ($\alpha = 10$ deg and $\beta = 0$) and the velocity-vector roll rate Ω_V varies from zero to 145 deg/s. The trim control inputs and the locus of eigenvalues are presented as functions of the velocity-vector roll rate Ω_V. The transition of the Dutch-roll-mode

---

**Data available online at http://www.nasa.gov/centers/dryden/history/pastprojects/HARV/Work/NASA2/nasa2.html [retrieved 9 Dec. 2007].
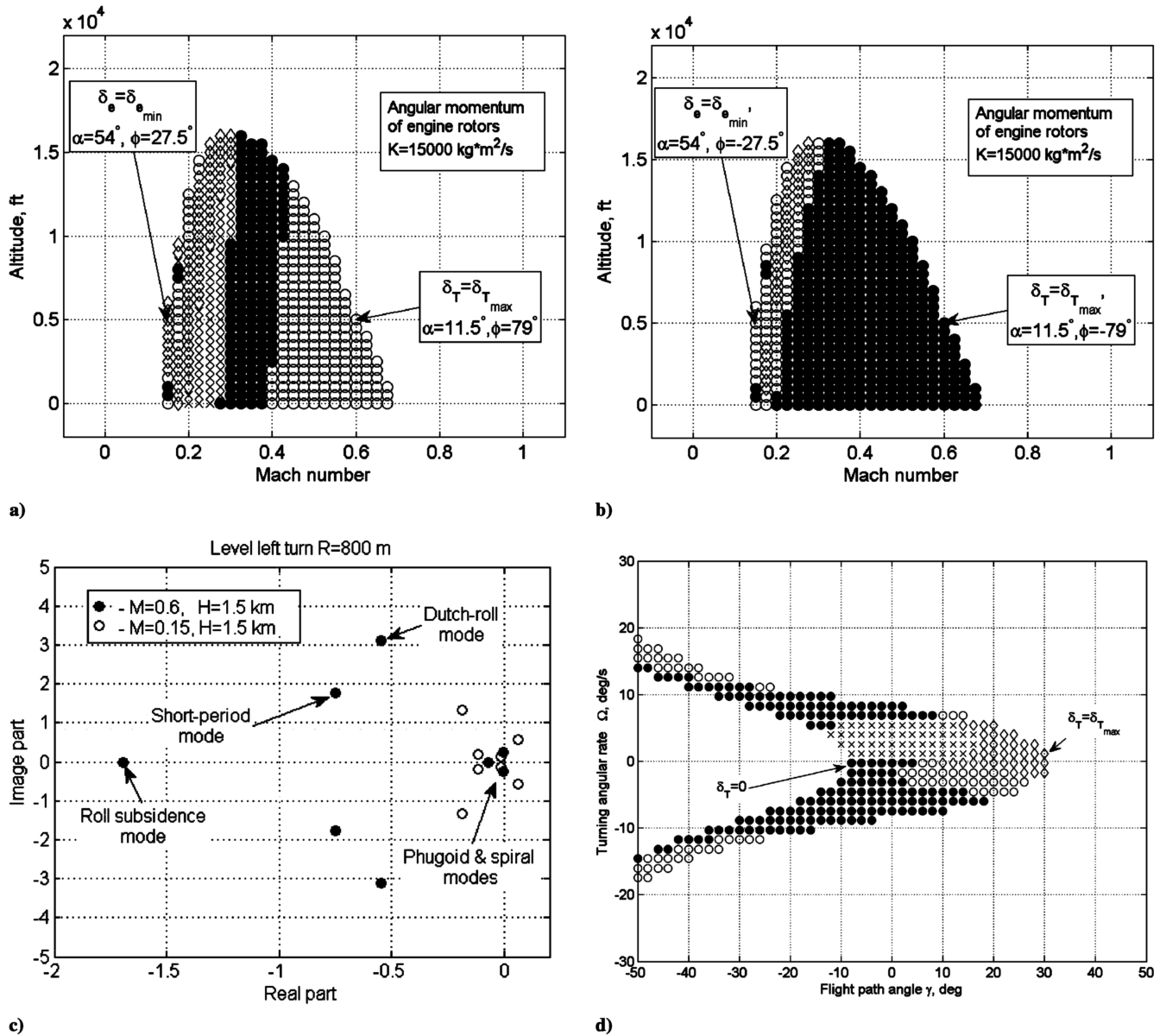
Fig. 3   F-18 HARV altitude-Mach number flight envelope for level turn ($\gamma = 0$) with $R = 800$ m and $\beta = 0$: a) right rotation, b) left rotation, c) eigenvalues for two steady turns with left rotation, and d) set of attainable steady helices for $H = 5$ km and $M = 0.4$.

eigenvalues to the right-hand side of the complex plane at $\Omega_V = 60$ deg/s indicates the Hopf bifurcation of the steady state. At $\Omega_V = 60$ deg/s, the steady states become oscillatory unstable and dynamics converge to stable limit-cycle oscillations (LCO). Qualitative analysis of the aircraft dynamics using attainable equilibrium sets and local stability maps can be effectively complemented by direct numerical simulation. However, this is out of the scope of the present paper.

B.   Aircraft B

The F-16 aircraft mathematical model used here as a second case study is based on the wind-tunnel low-speed aerodynamic data from [21], in which they were used in piloted simulation for investigation of the maneuvering characteristics and stall/poststall behavior of a relaxed static-stability airplane. The aerodynamic data cover a wide range of angles of attack (-20 to 90 deg) and sideslip angles (-30 to 30 deg). Most of the aerodynamic coefficients are interpolated using the two-dimensional data tables with angle of attack and sideslip as independent variables. The reduced aerodynamic data set derived from [21] for the F-16 model and the mass and inertia characteristics are presented in [2].

Figures 6a–6d show four cross sections of the attainable equilibrium states, similar to those shown in Figs. 4a–4d for

aircraft A. The same flight regime and graphical layout of computed cross sections allow consistent comparison of flight-mechanics parameters for different airframes. For example, at low angles of attack, aircraft A can be trimmed at higher sideslip angles, but its maximum attainable roll rate is approximately three times less than the maximum attainable role rate of aircraft B (Figs. 4a, 4b, 6a, and 6b). The maximum velocity-vector roll rate of aircraft A is limited due to saturation of the rudder and ailerons (Fig. 4b), whereas for aircraft B, the limiting factor is saturation of the elevator deflection (Fig. 6b). These two airframes have also different attainable steady-state regions in the Ω_V and β cross sections; they are presented in Figs. 4c, 4d, 6c, and 6d.

Aircraft A is aerodynamically stable at low angles of attack, whereas aircraft B is unstable in pitch at the same flight conditions at a reference location of the center of gravity $x_{cg} = 0.35\bar{c}$. Positive real eigenvalue $\lambda = 0.5$ rad/s (Fig. 7b) indicates the level of instability in pitch. The stability augmentation feedback control law can change the aircraft closed-loop eigenvalues and ensure stable dynamics. The control law gains will depend on the open-loop system eigenstructure, which can vary with a change of maneuver [30]. To illustrate this, the locus of eigenvalues and associated sequence of trim control inputs are presented in Figs. 7a and 7b as functions of velocity-vector roll rate Ω_V (the maneuver is specified by two arrows
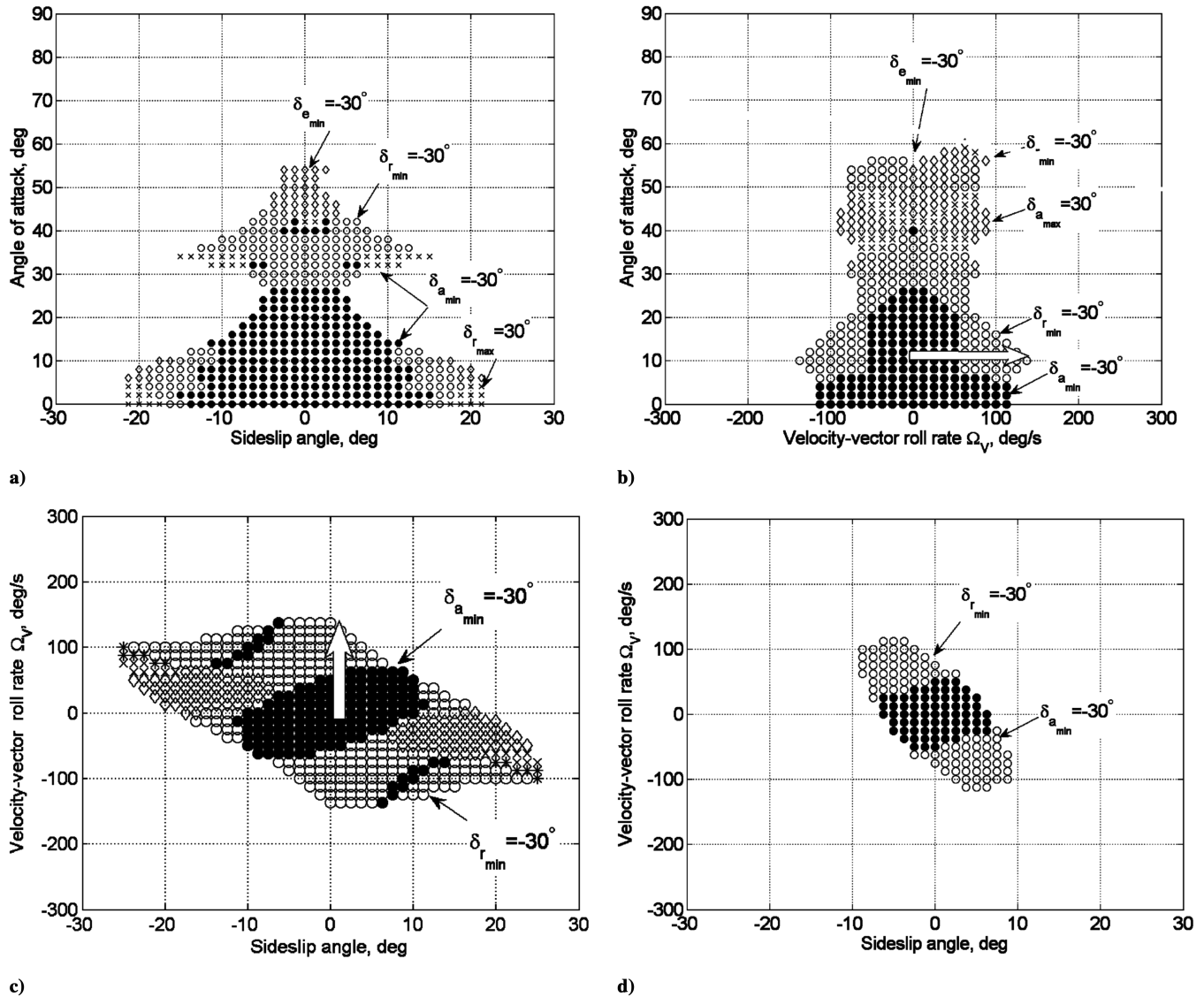
Fig. 4   F-18 HARV attainable equilibrium sets for the velocity-vector roll maneuver ($M = 0.4$ and $H = 5$ km) cross sections at a) $\Omega_V = 0$, b) $\beta = 0$, c) $\alpha = 10$ deg, and d) $\alpha = 20$ deg.

in Figs. 6b and 6c). The eigenvalues of an open-loop system during intensive roll maneuver due to inertia coupling are changed dramatically. In this example, there are two qualitative changes in the eigenvalues spectrum. The first one is when the unstable eigenvalue of the short-period mode moves to the stable semiplane with potential onset of the pitchfork bifurcation of steady states. Following this event, the system becomes stable for a small range of velocity-vector roll rates (Fig. 7a). But transition of the Dutch-roll-mode eigenvalues to the right-hand side of the semiplane makes the system unstable again. Note that after the Hopf bifurcation, the system will be attracted to the stable limit-cycle oscillations. The amplitude of these oscillations increases with the level of equilibrium instability.

At high angles of attack, the attainable steady-state regions shown in Fig. 6 are asymmetrical vs sideslip angle, due to asymmetry in the aerodynamic data. This asymmetry is quite typical for fighter aircraft configuration, due to onset of asymmetrical vortical flow structures, which are observed both in wind-tunnel tests and in flight. The cross section of the attainable equilibrium set presented in Fig. 6b indicates the existence of two groups of equilibrium states with positive and negative rotation at very high angles of attack. These equilibria represent aircraft flat-spin motion at zero sideslip with appropriate deflection of all control surfaces. The cross sections of the attainable equilibrium set, additionally computed for different values of

sideslip angle, reveal that these two steady-state "islands" are continuously connected with the "mainland" of steady states.

C.   Aircraft C

The third case study deals with the F-14 aircraft model, which is based on the wind-tunnel aerodynamic data from [22–24]. These data were used in piloted simulation for investigation of high-angle-of-attack maneuver-limiting factors. The aerodynamic model of the F-14 aircraft is also presented in [14], in which the aircraft nonlinear dynamics have been investigated using the continuation and bifurcation analysis methods. The aerodynamic data cover a wide range of angles of attack (0 to 90 deg) and sideslip angles (−20 to 20 deg), and they correspond to the wings fully swept forward. They are valid for low speeds ($M < 0.6$) and describe nonlinear dependencies of aerodynamic coefficients on angle of attack, sideslip angle, and elevator deflection.

Examples of the attainable equilibrium sets for aircraft C are shown in Figs. 8a–8d. They are computed for the same flight regime with cross sections similar to the two previous cases shown in Figs. 4a–4d for aircraft A and in Figs. 6a–6d for aircraft B. The attainable equilibrium regions in all cross sections have well-defined boundaries, which correspond to saturation of the rudder, ailerons, and elevator. At low angles of attack ($\alpha < 10$ deg), the attainable
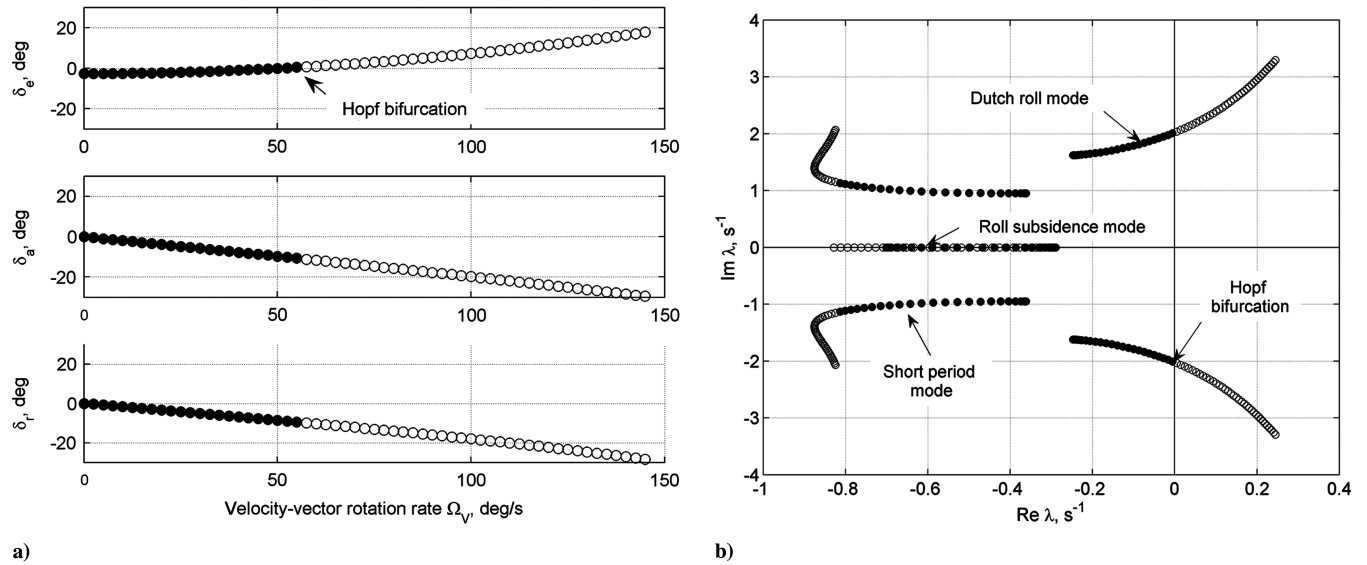
a)

b)

Fig. 5 F-18 steady-state maneuver specified by a selected sequence of equilibria with constant $\alpha = 10$ deg and $\beta = 0$ (see the arrows in Figs. 4b and 4c): a) trim deflections of control surfaces as functions of velocity-vector roll rate Ω_V and b) locus of eigenvalues.
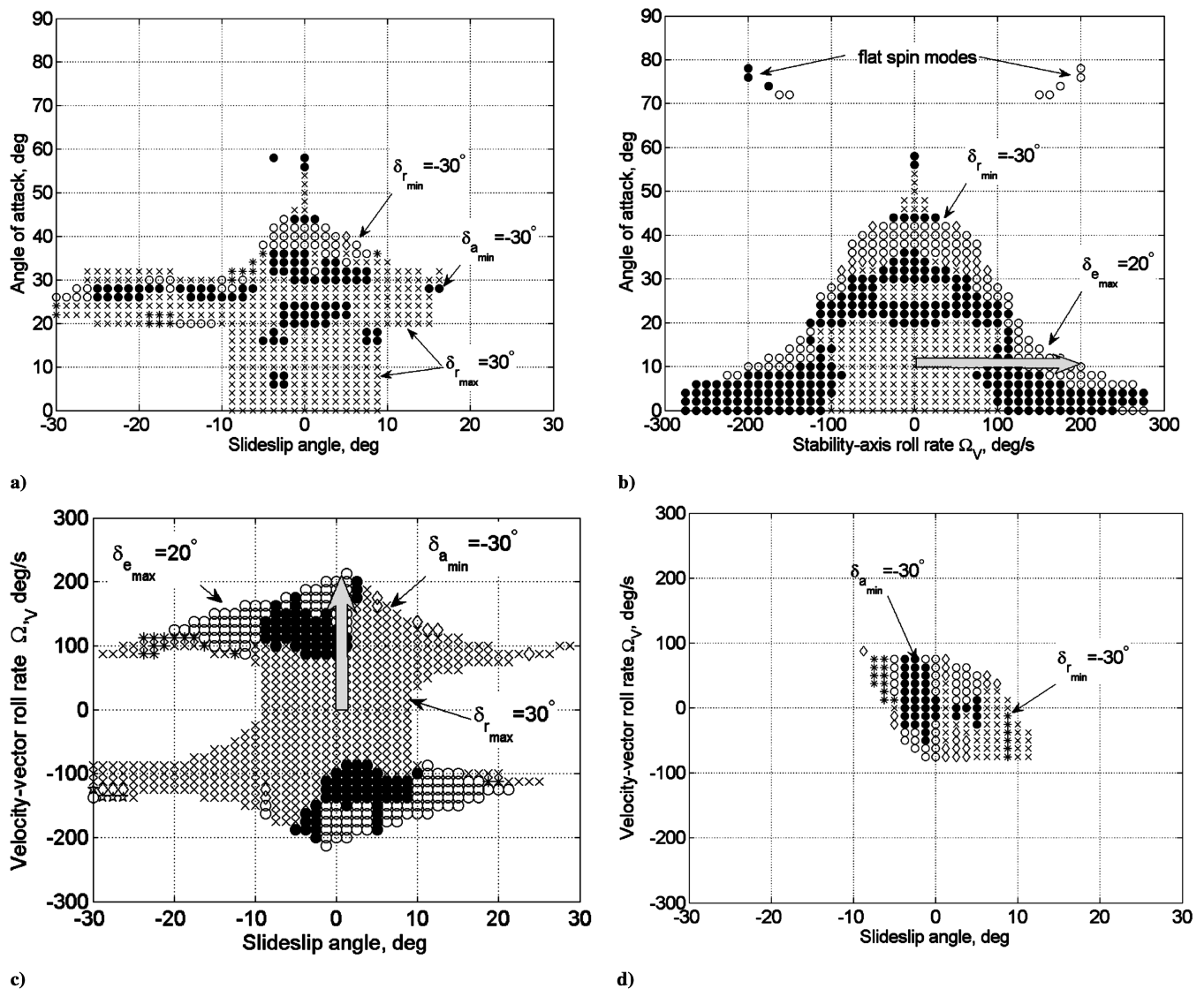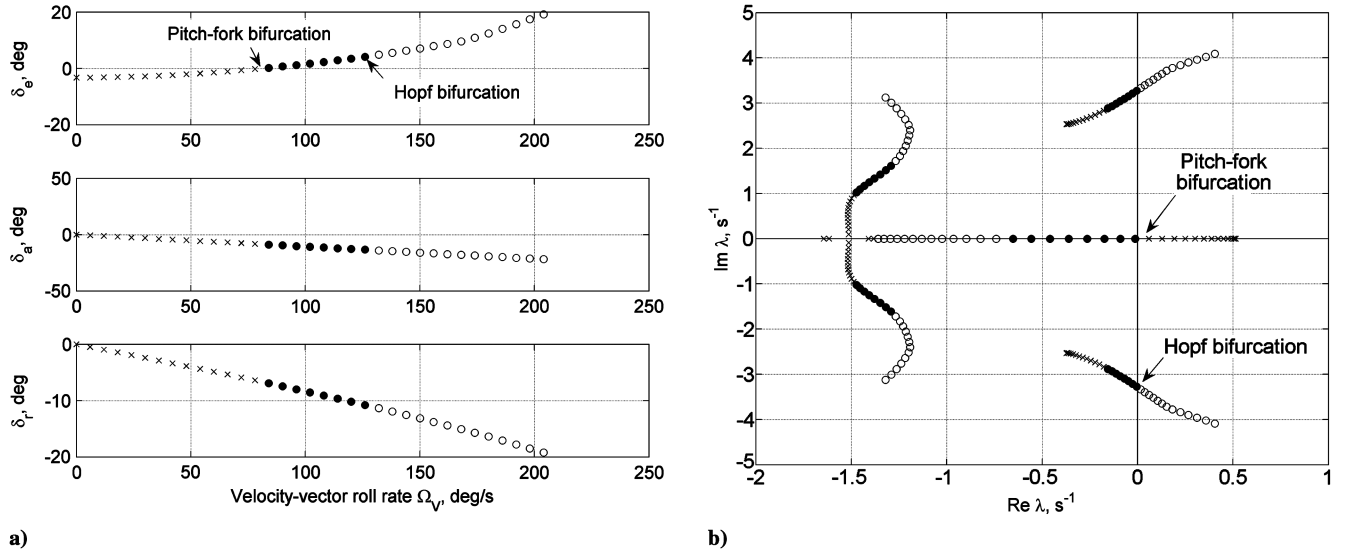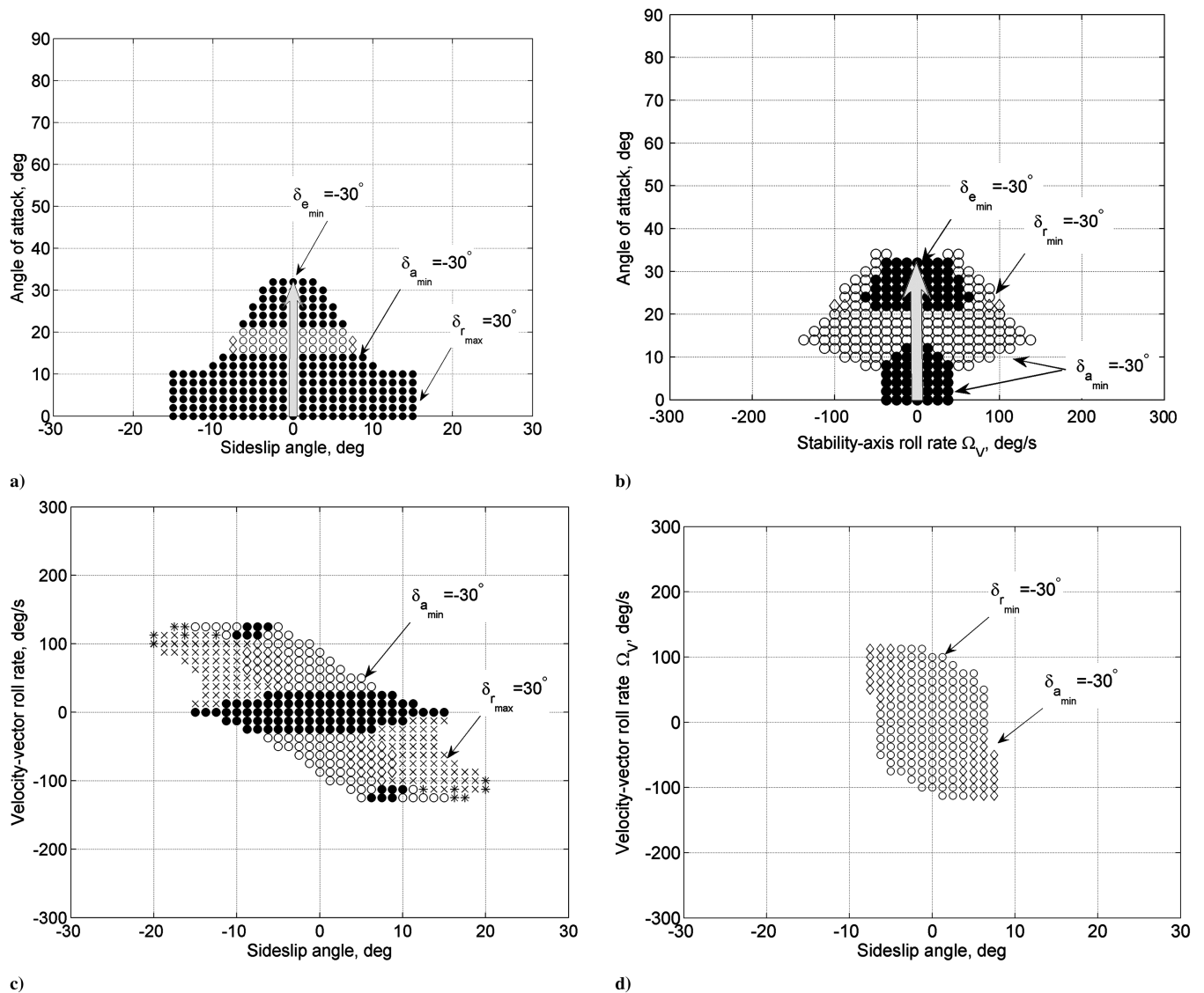

a)

b)

c)

d)

Fig. 6 F-16 attainable equilibrium sets for the velocity-vector roll maneuver ($M = 0.4$ and $H = 5$ km) cross sections at a) $\Omega_V = 0$, b) $\beta = 0$, c) $\alpha = 10$ deg, and d) $\alpha = 35$ deg.

a)   b)

Fig. 7   F-16 steady-state maneuver specified by a selected sequence of equilibria with constant $\alpha = 10$ deg and $\beta = 0$ (see the arrows in Figs. 6b and 6c):
a) trim deflections of control surfaces as functions of velocity-vector roll rate Ω_V and b) locus of eigenvalues.

a)   b)

c)   d)

Fig. 8   F-14 attainable equilibrium sets for the velocity-vector roll maneuver ($M = 0.4$ and $H = 5$ km) cross sections at a) $\Omega_V = 0$, b) $\beta = 0$,
c) $\alpha = 10$ deg, and d) $\alpha = 20$ deg.
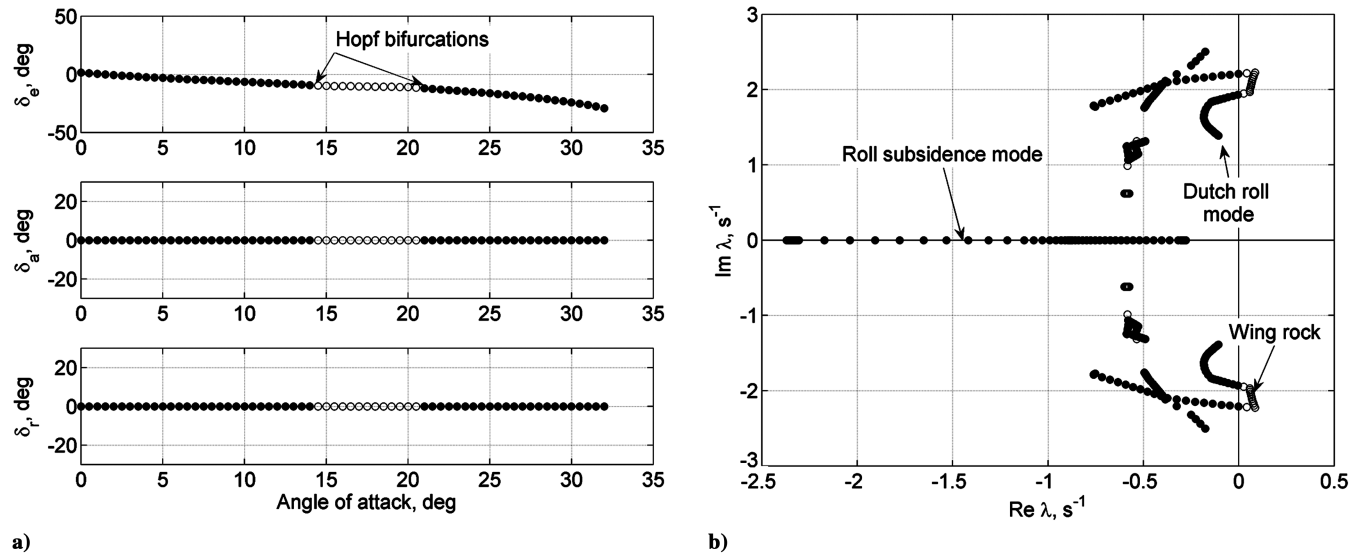
a)   **b)**

Fig. 9   **F-14 steady-state maneuver specified by a selected sequence of euqilibria with zero sideslip $\beta = 0$ and zero roll rate $\Omega_V = 0$ (see the arrows in Figs. 8a and 8b): a) trim deflections of control surfaces as functions of angle of attack α and b) locus of eigenvalues.**

range of sideslip angle ($|\beta| < 15$ deg) is bigger than in the case of aircraft B and less than in the case of aircraft A. However, the attainable range for the roll rate is much less ($|\Omega_V| < 40$ deg /s) than in the first two cases. There are two detached regions with stable steady states at low angles of attack ($\alpha < 14$ deg) and high angles of attack ($\alpha > 21$ deg). These two regions are separated by a region with oscillatory unstable steady states. Note that at high angles of attack, the maximum attainable roll rate significantly increases, but the steady states are oscillatory unstable (Fig. 8b). Performing longitudinal and velocity-vector roll maneuvers, the aircraft can enter the unstable region of steady states, which will produce a destabilizing effect on aircraft dynamics. For example, Fig. 9b shows the locus of eigenvalues for a longitudinal pull-up maneuver, denoted in Figs. 8a and 8b by vertical arrows, and Fig. 9a shows the associated control surface deflections. In the angle-of-attack range of 14 deg $\leq \alpha \leq 21$ deg, in which the Dutch roll mode eigenvalues are relocated to the right-hand-side semiplane, the aircraft will experience oscillatory instability in the lateral directional motion (Fig. 9b). There are two Hopf bifurcation points at $\alpha = 14$ and 21 deg (Fig. 9a), similar to the results presented in [14], in which they were obtained using the continuation method. The bifurcation parameters in our case are slightly different, because the speed is fixed according to selected flight regime $H = 5$ km and $M = 0.4$. The simulation results showing the buildup of the wing-rock amplitude are shown in [14]. The Hopf bifurcation will also take place when the aircraft is performing the velocity-vector roll maneuver, as was shown for aircraft A (Fig. 4b).

The computational time for one attainable equilibrium set in the form of a two-dimensional cross section depends on the size of the grid and also on the number of unattainable points. This is because each unattainable point will use the maximum number of iterations before moving to the next point. Attainable points can normally be converged in a few iterations. An average computation time for presented examples of attainable equilibrium sets with a grid of 40×40 points is about 15 min on a PC with an Intel© Centrino Duo processor.

V.   Conclusions

Consideration of the nonlinear models of the F-18 HARV, F-16, and F-14 aircraft allows us to conclude the following:

1) The computation of the set of all attainable steady states of the rigid aircraft equations of motion with imposed constraints assigning the maneuver type and its parameters provides a feasible and consistent way of investigating the nonlinear aircraft dynamics, which allows more efficient evaluation of the aircraft performance and maneuvering capabilities.

2) A number of representative attainable equilibrium sets computed on a two-dimensional grid of points in the maneuver parameter space can reveal a global structure of the multidimensional set of all steady states, which includes the aircraft maneuver limitations produced by saturation of control inputs and local stability properties in the form of stability maps.

3) The proposed method

a) possesses similarities and complementary features when compared with the bifurcation analysis method based on a one-parameter continuation of equilibrium states, and it is expected that the two approaches can be used in a complementary way.

b) can significantly facilitate the mathematical and piloted simulation methods by determining the critical regions of operation in which simulation is necessary to verify the model's dynamic behavior, and it can be used for comparative analysis of different airframes.

c) has a high potential for designing control laws (particularly for high-angle-of-attack flight and intensive roll maneuvers) via provision of interconnect schedules between different control surfaces, generation of linearized equations of motion consistent with performing maneuver, and postdesign evaluation of the designed control laws.

d) in combination with high-fidelity aircraft models validated in flight tests, will provide reliable quantitative results for actual performance and maneuvering capabilities.

References

[1] Etkin, B., *Dynamics of Atmospheric Flight*, Wiley, New York, 1972.
[2] Stevens, B. L., and Lewis, F. L., *Aircraft Control and Simulation*, 2nd ed., Wiley, New York, 2003.
[3] Pamadi, B. N., *Performance, Stability, Dynamics, and Control of Airplanes*, AIAA Education Series, AIAA, Reston, VA, 1998.
[4] Pashilkar, A. A., and Pradeep, S., "Computation of Flight Mechanics Parameters Using Continuation Techniques," *Journal of Guidance, Control, and Dynamics*, Vol. 24, No. 2, Mar.–Apr. 2001, pp. 324–329.

[5] Ananthkrishnan, N., and Sinha, N. K., "Level Flight Trim and Stability Analysis Using an Extended Bifurcation and Continuation Procedure," *Journal of Guidance, Control, and Dynamics*, Vol. 24, No. 6, 2001, pp. 1225–1228.

[6] Chudoba, B., and Cook, M. V., "Trim Equations of Motion for Aircraft Design: Turning Flight, Pull-Up and Push-Over," AIAA Atmospheric Flight Mechanics Conference and Exhibit, Austin, TX, AIAA Paper 2003-5693, 2003.

[7] Mehra, R. K., Kessel, W. C., and Carroll, J. V., "Global Stability and Control Analysis of Aircraft at High Angles of Attack," Scientific Systems, TR CR215-1, Cambridge, MA, 1977.

[8] Mehra, R. K., Kessel, W. C., and Carroll, J. V., "Global Stability and Control Analysis of Aircraft at High Angles of Attack," Scientific Systems, TR CR215-2, Cambridge, MA, 1978.

[9] Mehra, R. K., Kessel, W. C., and Carroll, J. V., "Global Stability and Control Analysis of Aircraft at High Angles of Attack," Scientific Systems, TR CR215-3, Cambridge, MA, 1979.

[10] Carroll, J. V., and Mehra, R. K., "Bifurcation Analysis of Nonlinear Aircraft Dynamics," *Journal of Guidance, Control, and Dynamics*, Vol. 5, No. 5, 1982, pp. 529–536.

[11] Paranjape, A., Sinha, N. K., and Ananthkrishnan, N., "Use of Bifurcation and Continuation Methods for Aircraft Trim and Stability Analysis—A State-of-the-Art," 45th AIAA Aerospace Scineces Meeting and Exhibit, Reno, NV, AIAA Paper 2007-1051, 2007.

[12] Guicheteau, P., "Bifurcation Theory Applied to the Study of Control Losses on Combat Aircraft," *La Recherche Aèrospatiale*, No. 2, 1982, pp. 61–73.

[13] Zagaynov, G. I., and Goman, M. G., "Bifurcation Analysis of Critical Aircraft Flight Regimes," International Council of Aerospace Sciences, Paper 84-4.2.1, 1984.

[14] Jahnke, C. C., and Culick, F. E. C., "Application of Bifurcation Theory to the High-Angle-of-Attack Dynamics of the F-14," *Journal of Aircraft*, Vol. 31, No. 1, 1994, pp. 26–34.

[15] Lowenberg, M. H., "Stability and Controllability Evaluation of Sustained Flight Manoeuvres," AIAA Atmospheric Flight Mechanics Conference, San Diego, CA, AIAA Paper 1996-3422, July 1996.

[16] Avanzini, G., de Matteis, G., and de Socio, L. M., "Aircraft Equilibrium and Response to Control in Intrinsic Coordinates," 35th Aerospace Sciences Meeting and Exhibit, Reno, NV, AIAA Paper 97-0323, Jan. 1997.

[17] Avanzini, G., and de Matteis, G., "Bifurcation Analysis of a Highly Augmented Aircraft Model," *Journal of Guidance, Control, and Dynamics*, Vol. 20, No. 4, 1997, pp. 754–759.

[18] Goman, M. G., Zagaynov, G. I., and Khramtsovsky, A. V., "Application of Bifurcation Theory to Nonlinear Flight Dynamics Problems," *Progress in Aerospace Sciences*, Vol. 33, No. 9, 1997, pp. 539–586.
doi:10.1016/S0376-0421(97)00001-8

[19] Goman, M. G., Patel, Y., and Khramtsovsky, A. V., "Flight Clearance Tools Using a Non-Linear Bifurcation Analysis Framework," AIAA Guidance, Navigation, and Control Conference and Exhibit, Austin, TX, AIAA Paper 2003-5557, 2003.

[20] Charles, G., Lowenberg, M., Stoten, D., Wang, X., and di Bernardo, M., "Aircraft Flight Dynamics Analysis and Controller Design Using Bifurcation Tailoring," AIAA Guidance, Navigation, and Control Conference and Exhibit, Monterey, CA, AIAA Paper 2002-4751, 2002.

[21] Nguyen, L. T., Ogburn, M. E., Gilbert, W. P., Kibler, K. S., Brown, P. W., and Deal, P. L., "Simulator Study of Stall/Post-Stall Characteristics of a Fighter Airplane with Relaxed Longitudinal Static Stability," NASA Langley Research Center TP 1538, Hampton, VA, 1979.

[22] Mitchell, D. G., Myers, T. T., Teper, G. L., Jonston, D. E., "Investigation of High-Angle-of-Attack Maneuver-Limiting Factors, Part 1: Analysis and Simulation,"U.S. Air Force, Wright Aeronautical Lab., TR-80-3141, Wright–Patterson AFB, OH, 1980.

[23] Mitchell, D. G., Myers, T. T., Teper, G. L., Jonston, D. E., "Investigation of High-Angle-of-Attack Maneuver-Limiting Factors, Part 2: Piloted Simulation Assessment of Bihrle Departure Criteria," U.S. Air Force Wright Aeronautical Lab., TR-80-3141, Wright–Patterson AFB, OH, 1980.

[24] Mitchell, D. G., Myers, T. T., Teper, G. L., Jonston, D. E., "Investigation of High-Angle-of-Attack Maneuver-Limiting Factors, Part 3: Appendices—Aerodynamic Models," U.S. Air Force Wright Aeronautical Lab., TR-80-3141, Wright–Patterson AFB, OH,1980.

[25] Durham, W. C., Lutze, F. H., and Mason, W., "Kinematics and Aerodynamics of Velocity-Vector Roll," *Journal of Guidance, Control, and Dynamics*, Vol. 17, No. 6, 1994, pp. 1228–1233.

[26] Young, J. W., Schy, A. A., and Johnson, K. G., "Pseudosteady-State Analysis of Nonlinear Aircraft Maneuvers," NASA Langley Research Center TP 1758, Hampton, VA, 1980.

[27] Guckenheimer, J., and Holmes, P., *Nonlinear Oscillations, Dynamical Systems, and Bifurcations of Vector Fields*, Springer–Verlag, New York, 1983.

[28] "Maneuver Limitations of Combat Aircraft," AGARD AGARD-AR-155A, 1979.

[29] Goman, M. G., Khramtsovsky, A. V., and Kolesnikov, E. N., "Investigation of the ADMIRE Manoeuvring Capabilities Using Qualitative Methods," *Nonlinear Analysis and Synthesis Techniques for Aircraft Control*, edited by D. Bates and M. Hagström, Lecture Notes in Control and Information Sciences, Vol. 365, 2007, Chap. 8, p. 360.

[30] Richardson, T. S., and Lowenberg, M. H., "A Continuation Design Framework for Nonlinear Flight Control Problems," *The Aeronautical Journal*, Vol. 110, No. 1104, 2006, pp. 85–96.